SCIENCE CHINA
Physics, Mechanics & Astronomy

•Article•

July 2022 Vol. 65 No. 7: 278211
https://doi.org/10.1007/s11433-022-1899-2

# Pressure-driven symmetry breaking and electron disproportionation of the trigonal $Nb_3$ cluster in $Nb_3Cl_8$

Zimin Jiang[1], Dequan Jiang[1], Yiming Wang[1], Chen Li[1], Ke Liu[1], Ting Wen[1], Fuyang Liu[1],
Zhengyang Zhou[2*], and Yonggang Wang[1*]

[1] *Center for High Pressure Science and Technology Advanced Research (HPSTAR), Beijing 100094, China;*
[2] *Shanghai Institute of Ceramics, Chinese Academy of Sciences, Shanghai 201899, China*

Received January 15, 2022; accepted March 29, 2022; published online May 27, 2022

Symmetry breaking of metal cluster-based strongly correlated systems can give rise to collective phenomena. Here, the two-dimensional $Nb_3$ cluster compound $Nb_3Cl_8$ is shown to suffer dramatic symmetry breaking and electron disproportionation under compression. A structural phase transition from trigonal $P\text{–}3m1$ to monoclinic $C2/m$ is observed near 8 GPa with the three-fold symmetry breaking. Electron disproportionation occurs on $Nb_3$ clusters from delocalized $Nb^{8/3+}Nb^{8/3+}Nb^{8/3+}$ to localized $Nb^{3+}Nb^{3+}Nb^{2+}$, which results in a subtle bandgap discontinuity, as evidenced by electrical transport and UV-Vis absorption measurements.

**$Nb_3Cl_8$, symmetry breaking, electron disproportionation, layered semiconductor, high pressure**

**PACS number(s):** 61.50.Ks, 71.20.Nr, 73.22.Gk, 62.50.+p

**Citation:** Z. Jiang, D. Jiang, Y. Wang, C. Li, K. Liu, T. Wen, F. Liu, Z. Zhou, and Y. Wang, Pressure-driven symmetry breaking and electron disproportionation of the trigonal $Nb_3$ cluster in $Nb_3Cl_8$, Sci. China-Phys. Mech. Astron. **65**, 278211 (2022), https://doi.org/10.1007/s11433-022-1899-2

## 1 Introduction

Transition metal cluster compounds have attracted great research interest regarding the discovery of new clusters and the key role of active metal sites in catalytic applications [1-5]. Among the numerous known metal cluster types, trigonal $M_3$ ($M$ = Ti, Nb, Ta, Mo, W, etc.) is the simplest but most significant representative [6-11]. These $M_3$ cluster compounds exhibit unusual magnetic properties due to the formation of intermetallic molecular orbitals of the equilateral trigonal metal ions accommodating the unpaired electrons. This characteristic leads to moment delocalization behavior similar to that of π-conjugated systems, which can introduce unusual magnetic behavior, such as valence bond condensation [12].

Materials with $M_3X_{13}$ units are the most studied series of trigonal $M_3$ clusters [13-17]. Geometric frustration and partial disappearance of spins were observed in $LiZn_2Mo_3O_8$ [18,19]. Several other $M_3X_{13}$ cluster compounds with antiferromagnetically interacted triangular lattices are recognized as spin-liquid candidates [20]. $M_3X_{13}$ units are also found in mixed-anion Nb/Ta/Mo/W compounds with electrons delocalized on the $M_3$ cluster [21-24]. Moreover, $Na_2Ti_3Cl_8$ presents a temperature-initiated nonpolar-to-polar trimerization transition at low temperature [25], in which the crystal structure transforms from isolated $Ti^{2+}$ ions to $[Ti_3]^{6+}$ clusters, coupled with a drastic magnetic susceptibility change [6]. The abovementioned phenomena demonstrate the $M_3$ cluster compounds as promising candidates for unusual quantum behavior and a unique platform for studies of structure-property relationships.

$Nb_3X_8$ ($X$ = Cl, Br, I) is one of the most representative among the numerous triangular cluster compounds [26-32].

---

*Corresponding authors (Zhengyang Zhou, email: zhouzhengyang@mail.sic.ac.cn; Yonggang Wang, email: yongang.wang@hpstar.ac.cn)

$Nb_3Cl_8$ with a two-dimensional $[Nb_3]^{8+}$ trimer layer is an insulator in ambient conditions, with each $[Nb_3]^{8+}$ trimer sharing one unpaired spin and forming an $S = 1/2$ antiferromagnetic triangular lattice. Upon cooling, $Nb_3Cl_8$ is also reported to exhibit a magnetic-to-nonmagnetic transition near 90 K, driven by the charge disproportionation from paramagnetic $[Nb_3]^{8+}[Nb_3]^{8+}$ to nonmagnetic $[Nb_3]^{7+}[Nb_3]^{9+}$ [26]. Partially replacing Cl with Br (i.e., $Nb_3Cl_{8-x}Br_x$) can systematically elevate the transition temperature from ~100 to ~400 K, and thus the optical properties [31]. McQueen's group [27] also reported the rearrangement of van der Waals stacking from a stacking manner of –AB–AB– to –AB′–BC′–CA′– and the formation of a singlet state during this magnetic transition. The dramatic symmetry lowering from $P$–3$m$1 to $C$2/$m$ coupled to the magnetic transition is considered to be responsible for the evasion of the geometric magnetic frustration to form a singlet ground state [27]. As one of the two fundamental thermodynamic variables besides temperature, pressure is also expected to be a powerful tool for altering the structural, electronic, and magnetic properties of strongly correlated systems [33,34]. However, the effect of pressure on the crystal structure and electric/magnetic behaviors of trigonal $Nb_3$ cluster compounds has not been reported yet.

In this paper, two-dimensional $Nb_3Cl_8$ is used to investigate the geometric and electric stabilities of an $S = 1/2$ $M_3$ cluster under high pressure (HP). Surprisingly, $Nb_3Cl_8$ does not undergo a layer stacking phase transition or an interlayer charge disproportionation upon cooling. Instead, three-fold symmetry breaking was observed during a pressure-induced phase transition from $P$–3$m$1 to $C$2/$m$ near 8 GPa, accompanied by an intra-$Nb_3$-cluster electron disproportionation. By combining the extensive *in situ* HP techniques, a preliminary structure-property relationship of $Nb_3Cl_8$ under compression is proposed. The similar but distinct effects of temperature and pressure on the trigonal $Nb_3$ cluster are discussed accordingly.

## 2 Materials and methods

All chemicals were of reagent grade quality with no further purification. $Nb_3Cl_8$ powders were synthesized by direct solid-state reaction of stoichiometric Nb and $NbCl_5$ powders at 700°C in sealed quartz tubes for 24 h. The powder samples were characterized at atmospheric pressure using a Cu Kα radiation X-ray diffraction (XRD) diffractometer. The *in situ* HP measurement was generated by a pair of anvils with a 400 μm diamond anvil cell, the thickness of the steel gasket was approximately 30 μm, the diameter of the sample chamber was 180 μm, and the sample and ruby ball were placed in the sample chamber, adopting the fluorescence peak calibration pressure based on the ruby ball.

*In situ* HP room temperature XRD characteristics were measured using a monochromatic X-ray beam at a wavelength of 0.6199 Å at the 4W2 High-pressure Station in the Beijing Synchrotron Radiation Facility (BSRF), with $CeO_2$ acting as the calibration standard. DIOPTAS [35] software was used to perform data reduction, and the Rietveld method in FULLPROF [36] software was used to refine the cell parameters under different pressures.

*In situ* UV-Vis absorption spectra were measured using a home-designed spectroscopy system with a Xeon light source between 300 and 1100 nm in the micro area (Gora-UVN-FL, built by Ideaoptics, Shanghai, China). Silicone oil was used as the pressure transmission medium. The bandgap was determined by extrapolating the linear part of the $(\alpha h\nu)^{1/2}$ and $h\nu$ curve, where $\alpha$ is the absorption coefficient, $h$ is Planck's constant, and $\nu$ is the frequency of the photon.

*In situ* HP Raman spectra of the $Nb_3Cl_8$ powders were obtained with a 532 nm, 1.73 mW laser. NaCl was used as the pressure transmission medium. A conventional four-point-probe method was used to perform electrical transport measurements on a home-designed, low-temperature electric transport test system, with a cubic boron nitride layer placed between the steel gasket and the anvil diamond to provide electrical insulation for the electrical leads and steel gasket. The Au electrodes were attached to the sample in the chamber, and an electric current of 1 mA was used for the resistance measurement.

## 3 Results and discussion

Figure 1(a) presents the ambient structure of $Nb_3Cl_8$ crystallizing in a van der Waals type of packing with trigonal space group $P$–3$m$1. The crystal structure can be considered stacked $[Nb_3]^{8+}Cl_8$ layers along the $c$-axis in an –AB–AB– manner. The $S = 1/2$ triangular $Nb_3$ clusters further form a triangular lattice in the $ab$ plane. The molecular orbitals of this trigonal and intermetallic $Nb_3$ cluster are presented in Figure 1(b). The formation of the $Nb_3$ trimer is evident from the short Nb–Nb metal bonding of ~2.81 Å versus the longer Nb–Nb metal bond of ~3.92 Å, and all Nb atoms are located on the equivalent crystallographic sites (6$i$). The central Nb atoms are surrounded by six Cl atoms, and the $[NbCl_6]$ octahedra link each other by edge-sharing to give the infinite $[Nb_3]^{8+}Cl_8$ layers (Figure 1(c)). The apparent valence state of the $Nb_3$ cluster in $Nb_3Cl_8$ in ambient conditions is $(Nb^{8/3+}Nb^{8/3+}Nb^{8/3+})$. The molecular orbitals of $Nb_3Cl_8$ are depicted in Figure 1(d), with the $3 \times t_{2g}$ orbitals reorganized into four bonding orbitals ($1e + 1a_1 + 2a_1$) and five antibonding orbitals ($2e + 1a_2 + 3e$). The seven $d$ electrons of the $Nb_3$ trimer are distributed in the three bonding orbitals, with one unpaired electron in the nonbonding orbital. Consequently, all three Nb atoms within a $Nb_3$ trimer share one

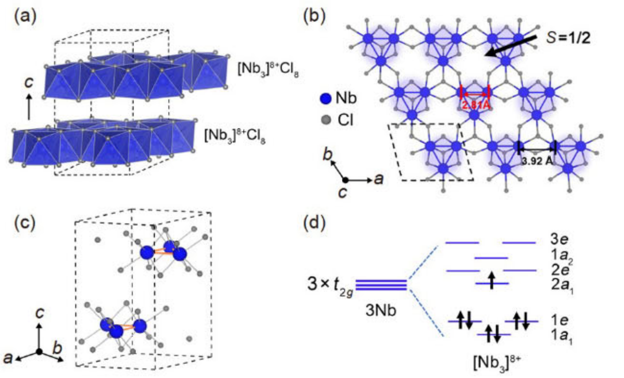

**Figure 1** (Color online) (a) Stacking layer structure of $Nb_3Cl_8$; (b) $Nb_3Cl_8$ trimers forming the triangular lattice; (c) $Nb_3Cl_{13}$ unit; (d) schematic view of the molecular orbitals formed in a $Nb_3$ trimer with the ground-state electron configuration.

unpaired electron, leading to an $S = 1/2$ moment on each $Nb_3$ cluster.

Figure 2(a) shows the evolution of *in situ* HP XRD of $Nb_3Cl_8$ at room temperature with silicone oil as the pressure transmission medium. Almost all XRD peaks at 0.6 GPa can be indexed into the trigonal space group *P*–3*m*1 corresponding to the low-pressure (LP) structure of $Nb_3Cl_8$. Upon compression, the (002) and (100) peaks approach each other slowly and finally merge near 6.5 GPa, suggesting a structural transformation. Figure 2(b) shows the cell parameters (*a*, *c*, and *a*/*c*) determined by LeBail fitting of *in situ* HP XRD, in which a structural phase transformation from trigonal *P*–3*m*1 for the LP phase to monoclinic *C*2/*m* for the HP phase is evident during compression near 7-8 GPa. The LeBail fitting results at selected pressures and the volume evolution of $Nb_3Cl_8$ as a function of pressure are provided in Figures S2 and S3 (Supporting Information). The determination of the space group for HP-$Nb_3Cl_8$ is based on the combination of indexing the powder and single-crystal XRD and Raman spectra. Figure 2(c) shows the Rietveld refinement result of HP-$Nb_3Cl_8$ at 9.7 GPa using the proposed *C*2/*m* structure. The experimental data show good agreement with the theoretical pattern (except a small peak at ~10° from unknown purity), confirming the rationality of the HP structure (Figure S4 and Table S1).

Transitions of properties are expected to be the same or similar, whether they are driven by pressure or temperature. $Nb_3Cl_8$ suffers a dramatic charge disproportionation from paramagnetic $[Nb_3]^{8+}[Nb_3]^{8+}$ to nonmagnetic $[Nb_3]^{7+}[Nb_3]^{9+}$ near 100 K [26]. Surprisingly, despite having the same space group *C*2/*m*, the crystal structure of HP-$Nb_3Cl_8$ is distinct from the low-temperature structure of $Nb_3Cl_8$ with disproportionated $Nb_3Cl_8$ layers with $[Nb_3]^{7+}Cl_{13}$ and $[Nb_3]^{9+}Cl_{13}$ clusters. Alternatively, $Nb_3Cl_8$ suffers an anomalous $D_{3d}$ symmetry breaking during the pressure-induced LP-to-HP phase transition.

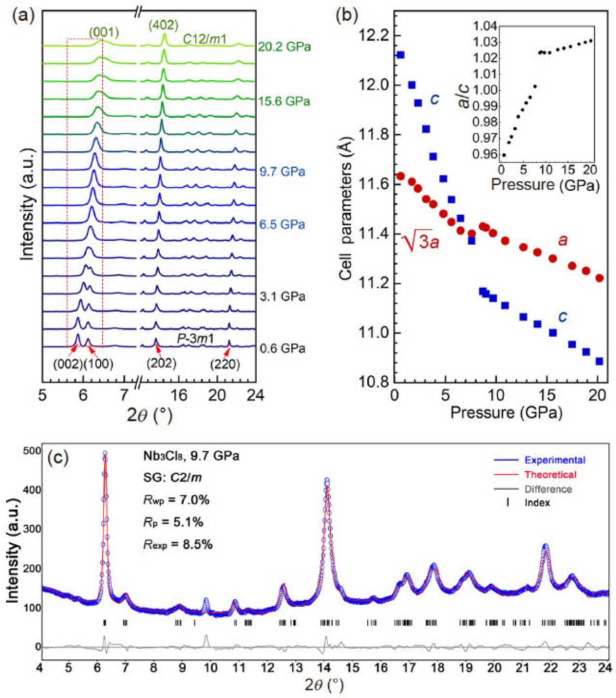

**Figure 2** (Color online) (a) Powder XRD patterns of $Nb_3Cl_8$ under compression up to 20.2 GPa. (b) Cell parameters of $Nb_3Cl_8$ as a function of pressure. Inset shows the trend of *a*/*c* under compression. (c) Rietveld refinement result of the HP phase of $Nb_3Cl_8$ at 9.7 GPa using the proposed *C*2/*m* structure.

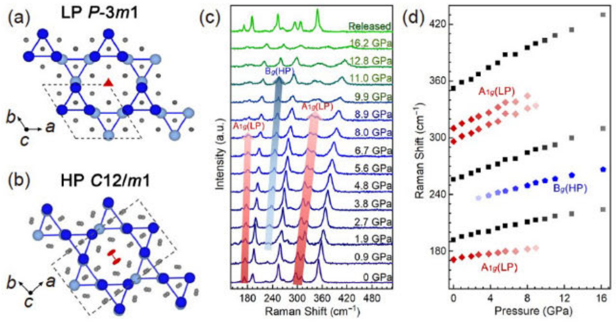

**Figure 3** (Color online) Crystal structures of (a) the LP phase and (b) the HP phase of $Nb_3Cl_8$ viewed along the *c*-axis. The red symmetry elements show the characteristic features of the LP and HP structures. (c) Raman spectra of $Nb_3Cl_8$ as a function of pressure. The red and blue arrows show the subtle changes of characteristic Raman modes of $A_{1g}$ for the LP phase and $B_g$ for the HP phase, respectively. (d) Pressure dependence of the Raman peak position.

Figure 3(a) and (b) show the essential structural features of the LP and HP phases of $Nb_3Cl_8$. The LP/ambient structure adopts the trigonal space group *P*–3*m*1 with 3-fold rotational symmetry around the *c*-axis. The three Nb atoms on the $Nb_3$ clusters are of the same coordination environment, with an apparent valence state of $Nb^{8/3+}$ and one unpaired electron delocalized above them. In this case, the formation of intermetallic $Nb_3$ molecular orbitals can reduce the total energy efficiently, and the $S = 1/2$ $Nb_3$ clusters can further form a triangular lattice, giving rise to geometric frustration. Under compression, this ground state is destroyed by $D_{3d}$ symmetry breaking to $C_{2h}$ in monoclinic space group $C2/m$, with the disproportionation of Nb–Nb bond lengths within the $Nb_3$ clusters. The emerging 2-fold rotation axes are located at the center of the monoclinic unit cell of the HP phase, and the apparent valence states of Nb are ($Nb^{3+}Nb^{3+}Nb^{2+}$). Consequently, the one unpaired electron is localized on one of the three Nb atoms of the $Nb_3$ cluster, and the $S = 1/2$ frustrated lattice no longer exists in the HP phase of $Nb_3Cl_8$.

Figure 3(c) and (d) display the *in situ* Raman spectra of $Nb_3Cl_8$ under compression. On the basis of group theory [31,37-43], the mechanical-vibrational representation of LP $Nb_3Cl_8$ ($P–3m1$, point group $D_{3d}$) can be written as $M = 8A_{1g} + 3A_{1u} + 3A_{2g} + 8A_{2u} + 11E_u + 11E_g$. This representation includes $\Gamma_{\text{acoustic}} = A_{2u} + E_u$ and $\Gamma_{\text{optic}} = 8A_{1g} + 3A_{1u} + 3A_{2g} + 7A_{2u} + 10E_u + 11E_g$, in which the odd ($u$) vibrational modes are IR-active, and the even ($g$) vibrational modes are Raman-active. Thus, the IR-active modes are $7A_{2u} + 10E_u$ and the Raman-active modes are $8A_{1g} + 11E_g$ for LP $Nb_3Cl_8$. In particular, the $A_{1g}$ mode is recognized as closely related to the unpaired $d$ electron of the trigonal $Nb_3$ trimer [18]. In contrast, the mechanical-vibrational representation of the HP phase of $Nb_3Cl_8$ ($C2/m$, point group $C_{2h}$) is $M = 19A_g + 14A_u + 14B_g + 19B_u$, including $\Gamma_{\text{acoustic}} = A_u + 2B_u$ and $\Gamma_{\text{optic}} = 19A_g + 13A_u + 14B_g + 17B_u$. The Raman-active modes are $19A_g + 14B_g$. The characteristic table of the $D_{3d}$ and $C_{2h}$ point groups is provided in Tables S2 and S3, respectively.

The experimental Raman changes are particularly consistent with the theoretical vibrational analyses based on group theory. The ambient Raman spectra are dominated by six peaks, with three $A_{1g}$ modes located at 172, 296, and 310 $cm^{-1}$. Under compression, the intensities of the $A_{1g}$ peaks decrease gradually, indicating the partial breaking of the original $D_{3d}$ symmetry. Meanwhile, a Raman peak located near 238 $cm^{-1}$ grows, which is identified as the $B_g$ mode of HP-$Nb_3Cl_8$. The phenomenon of one Raman mode weakening/disappearing and the other growing proves the symmetry change from a trigonal $Nb_3$ cluster to the monoclinic HP phase with electron disproportionation. The onsets of the Raman mode changes occur far before the phase transition, as evidenced by XRD data (near 8 GPa), which is reasonable considering the distinct features of a structural phase transition characterized on an average atomic level (XRD) or a local structure level (Raman).

As a consequence of $D_{3d}$ symmetry breaking and the disproportionation of the Nb–Nb bond lengths, the apparent valence state of the $Nb_3$ cluster in $Nb_3Cl_8$ changes from ($Nb^{8/3+}Nb^{8/3+}Nb^{8/3+}$) in ambient conditions to ($Nb^{3+}Nb^{3+}Nb^{2+}$) at HPs. Electron location functions (ELFs) of the LP and HP phases of $Nb_3Cl_8$ are calculated to visually describe the evolution of the electron distribution on Nb3 clusters. As shown in Figure 4(a), the electron density is evenly distributed over the three Nb atoms of $Nb_3$ trimers in LP-$Nb_3Cl_8$, and intermetallic Nb–Nb bonding forms between adjacent Nb centers because of the delocalization of the one unpaired electron. Meanwhile, the ELF of HP-$Nb_3Cl_8$ in Figure 4(b) shows an evident difference among the Nb atoms located on the two distinct Wyckoff sites. The unpaired $d$ electron is apparently localized on Nb2, and the original equal distribution of the one spin above three Nb atoms is destroyed.

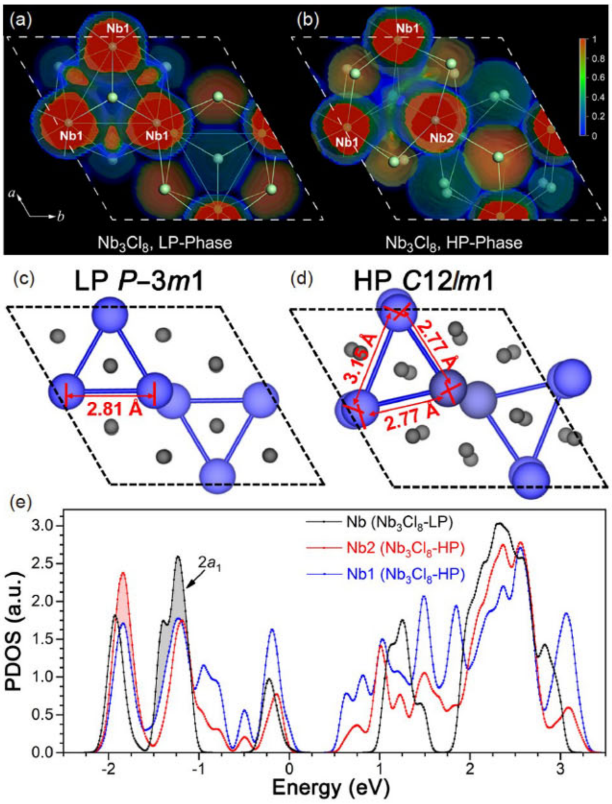

**Figure 4** (Color online) ELF of (a) the LP phase of $Nb_3Cl_8$ in the (004) plane and (b) the HP phase (9.7 GPa) of $Nb_3Cl_8$ in the (004) plane; bond length changes of the $Nb_3$ trimer within (c) the LP structure and (d) HP structure (9.7 GPa) of $Nb_3Cl_8$; (e) partial density of states of Nb in the LP phase of $Nb_3Cl_8$ and Nb1/Nb2 in the HP phase of $Nb_3Cl_8$.

The degeneration of the intermetallic Nb–Nb bonding in Figure 4(c) and (d) yields a dramatic bond length change from three Nb–Nb bonds of 2.81 Å to two short Nb–Nb bonds of 2.77 Å and one longer Nb–Nb bond of 3.15 Å in LP- and HP-$Nb_3Cl_8$, respectively. The DFT molecular orbital calculations in Figure 4(e) using LDA + $U$ (with $U$ =4 eV [27]) also suggest a dramatic change in the shared $2a_1$ molecular orbital of the $Nb_3$ cluster with a $D_{3d}$ symmetry to a degenerated orbital of the Nb2 atom only. Although we have proposed a $Nb^{8/3+}Nb^{8/3+}Nb^{8/3+}$ to $Nb^{3+}Nb^{3+}Nb^{2+}$ charge disproportionation across the LP-to-HP phase transition, electron overlapping and metallic bonding still occur between Nb1 and Nb2, as well as Nb1 and Nb1, instead of a thorough ionization (Figure S5).

The phenomena of symmetry breaking and electron localization or delocalization are essential to determine the collective physical properties of a strongly correlated system.

Most semiconductors will suffer an insulator-to-metal transition under compression [44-46]. In very few cases, metallic materials can undergo an inverse change from metal to insulator via a bandgap opening [32]. In ambient conditions, electron delocalization (intra-cluster) and electron localization (inter-cluster) occur in layered $Nb_3Cl_8$, the latter of which causes the material to exhibit semiconducting behavior and a greenish color. Therefore, it is difficult to predict the effect of compression on the physical properties of $Nb_3Cl_8$ accompanied by the localization of the one unpaired electron of $Nb_3$ clusters. Figure 5(a) displays the electrical resistance of $Nb_3Cl_8$ as a function of temperature and pressure. $Nb_3Cl_8$ shows relatively large resistances and semiconducting behavior from 0.9 to 22 GPa (Figure S6), which rules out the insulator-to-metal transition during the pressure-induced structural phase transition and electron localization. The bandgap $E_g$ of $Nb_3Cl_8$ can be derived according to the equation:

$$\ln R(T) = E_g / 2k_g T. \tag{1}$$

A clear decrease (~13.9%) in $E_g$ is observed near 6-7 GPa from the normalized $E_g/E_{g0}$ curve, corresponding to the pressure-induced phase transition but with the semiconducting behavior retained in the HP phase.

*In situ* UV-Vis absorption spectra are used to double-check the bandgap change of $Nb_3Cl_8$ under compression. $Nb_3Cl_8$ is a proven indirect bandgap semiconductor in ambient conditions, with an absorption edge near 330 nm (3.8 eV). Unlike most of the other semiconductors exhibiting piezochromicity under HP [47-50], $Nb_3Cl_8$ undergoes only a subtle redshift, as shown in the UV-Vis absorption spectra near 8 GPa (Figure 5(b)). Likewise, the fitted bandgap values show a tiny (0.09 eV) but sudden decrease near 8 GPa (Figures 5(c) and S7). LP- and HP-$Nb_3Cl_8$ show an almost unchanged greenish color through the pressure-induced phase transition, which also confirms the semiconducting behavior of the HP phase of $Nb_3Cl_8$.

The effect of pressure on the structural and physical properties of $M_3$ cluster compounds is interesting. Previous studies have demonstrated that temperature and chemical doping can introduce interlayer charge disproportionation and phase transitions, respectively, altering the arrangement of the layers composed of $M_3$ clusters. Pressure can undoubtedly result in similar but distinct phenomena associated with symmetry breaking and electron/spin localization, which will destroy the basic feature of a layered $M_3$ cluster compound: the 3-fold rotational symmetry axis. Possible magnetic ordering is expected after the breaking of geometric frustration. Multistep transitions, such as an insulator-to-semiconductor transition, followed by a final metallization are also expected in an $M_3$ cluster compound under HP.

## 4 Conclusions

In summary, we reported the pressure-induced structural phase transformation, symmetry breaking, and electron localization in a $Nb_3$ cluster compound, $Nb_3Cl_8$. The van der Waals crystal $Nb_3Cl_8$ undergoes a structural transition from trigonal $P$–3$m$1 to monoclinic $C2/m$ near 7-8 GPa. The most significant consequence of this pressure-induced phase transition is the breaking of the $D_{3d}$ symmetry of $Nb_3$ clusters and electron delocalization of the one unpaired electron. Raman spectra and ELF calculations further confirm the symmetry change and electron disproportionation within the $Nb_3$ cluster under compression. $Nb_3Cl_8$ shows subtle changes in the electrical transport and UV-Vis absorption spectra along with the structural phase transition. These results

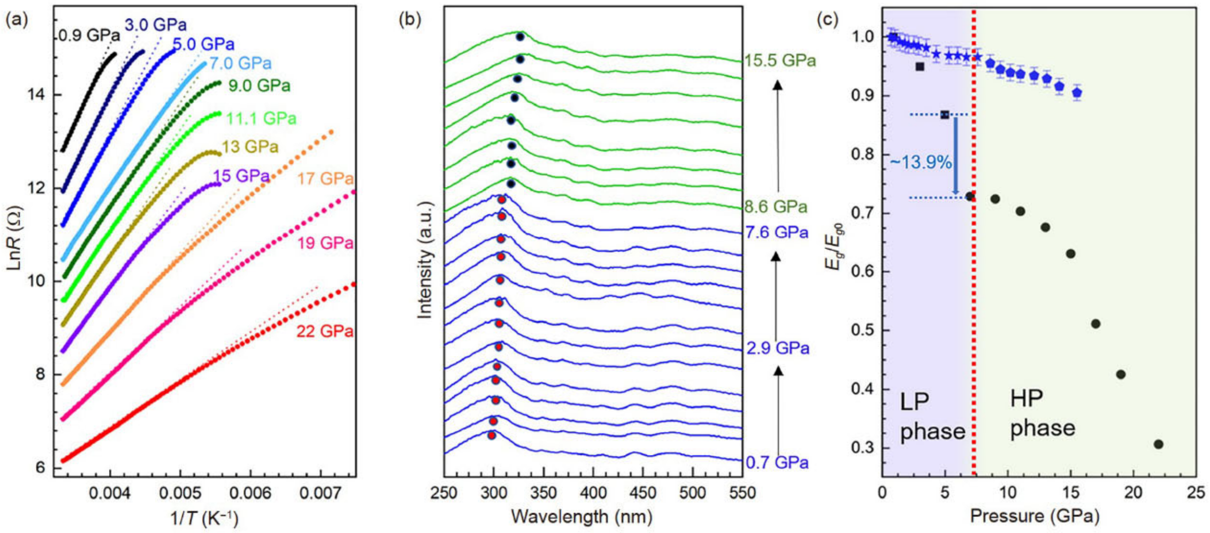

**Figure 5** (Color online) (a) Electrical transport behaviors of $Nb_3Cl_8$ under compression; (b) UV-Vis absorption spectra of $Nb_3Cl_8$ under compression; (c) evolution of $E_g/E_{g0}$ based on electrical transport and UV-Vis absorption spectra under compression.

provide novel evidence and a deep understanding of the effect of pressure on the structural and electrical properties of $M_3$ cluster compounds.

*This work was supported by the National Natural Science Foundation of China (Grant No. 52073003), the Major Program of National Natural Science Foundation of China (Grant No. 22090041), the National Key R&D Program of China (Grant No. 2018YFA0305900), and the Shanghai Sailing Program (Grant No. 21YF1454400). HP XRD data were collected at the 4W2 High-pressure Station in the Beijing Synchrotron Radiation Facility (BSRF).*

**Supporting Information**

The supporting information is available online at http://phys.scichina.com and https://link.springer.com. The supporting materials are published as submitted, without typesetting or editing. The responsibility for scientific accuracy and content remains entirely with the authors.

1 A. Müller, R. Jostes, and F. A. Cotton, Angew. Chem. Int. Ed. **19**, 875 (1980).

2 J. W. Lauher, J. Am. Chem. Soc. **16**, 5306 (1978).

3 F. A. Cotton, Inorg. Chem. **3**, 1217 (1964).

4 P. Lemoine, J.-F. Halet, and S. Cordier, *Inorganic Niobium and Tantalum Octahedral Cluster Halide Compounds with Three-Dimensional Frameworks: A Review on Their Crystallographic and Electronic Structures* (Springer, Cham, 2019). p. 143.

5 F. A. Cotton, and G. G. Stanley, Chem. Phys. Lett. **58**, 450 (1978).

6 D. J. Hinz, G. Meyer, T. Dedecke, and W. Urland, Angew. Chem. Int. Ed. Engl. **34**, 71 (1995).

7 M. A. Walters, K. C. Lam, S. Damo, R. D. Sommer, and A. L. Rheingold, InOrg. Chem. Commun. **3**, 316 (2000).

8 G. J. Miller, J. Alloys Compd. **229**, 93 (1995).

9 B. Wang, H. J. Zhai, X. Huang, and L. S. Wang, J. Phys. Chem. A **112**, 10962 (2008).

10 S. J. Hibble, S. P. Cooper, A. C. Hannon, S. Patat, and W. H. McCarroll, Inorg. Chem. **37**, 6839 (1998).

11 M. P. Doyle, M. R. Colsman, and M. S. Chinn, Inorg. Chem. **23**, 3684 (1984).

12 J. Guevara, F. Parisi, A. M. Llois, and M. Weissmann, Phys. Rev. B **55**, 13283 (1997).

13 P. Gall, R. A. Rahal Al Orabi, T. Guizouarn, and P. Gougeon, J. Solid State Chem. **208**, 99 (2013).

14 P. Gall, and P. Gougeon, Acta Cryst. **72**, 995 (2016).

15 K. E. Sandvik, D. Okuyama, K. Nawa, M. Avdeev, and T. J. Sato, J. Solid State Chem. **271**, 216 (2019), arXiv: 1901.02171.

16 P. Gall, R. A. R. A. Orabi, T. Guizouarn, J. Cuny, B. Fontaine, R. Gautier, and P. Gougeon, J. Solid State Chem. **201**, 312 (2013).

17 C. C. Torardi, and R. E. McCarley, Inorg. Chem. **24**, 476 (1985).

18 J. P. Sheckelton, J. R. Neilson, D. G. Soltan, and T. M. McQueen, Nat. Mater. **11**, 493 (2012), arXiv: 1303.6986.

19 R. Flint, and P. A. Lee, Phys. Rev. Lett. **111**, 217201 (2013), arXiv: 1308.2642.

20 Y. Haraguchi, C. Michioka, H. Ueda, and K. Yoshimura, Chem. Eur. J. **23**, 15879 (2017).

21 E. Babaian-Kibala, F. A. Cotton, and M. Shang, Inorg. Chem. **29**, 5148 (1990).

22 G. V. Khvorykh, A. V. Shevelkov, V. A. Dolgikh, and B. A. Popovkin, J. Solid State Chem. **120**, 311 (1995).

23 F. A. Cotton, M. Shang, and Z. S. Sun, J. Am. Chem. Soc. **113**, 3007 (1991).

24 H. J. Zhai, B. Wang, X. Huang, and L. S. Wang, J. Phys. Chem. A **113**, 9804 (2009).

25 Z. A. Kelly, T. T. Tran, and T. M. McQueen, Inorg. Chem. **58**, 11941 (2019).

26 Y. Haraguchi, C. Michioka, M. Ishikawa, Y. Nakano, H. Yamochi, H. Ueda, and K. Yoshimura, Inorg. Chem. **56**, 3483 (2017).

27 J. P. Sheckelton, K. W. Plumb, B. A. Trump, C. L. Broholm, and T. M. McQueen, Inorg. Chem. Front. **4**, 481 (2017).

28 J. R. Kennedy, and A. Simon, Inorg. Chem. **30**, 2564 (1991).

29 J. Yoon, E. Lesne, K. Sklarek, J. Sheckelton, C. Pasco, S. S. P. Parkin, T. M. McQueen, and M. N. Ali, J. Phys.-Condens. Matter **32**, 304004 (2020), arXiv: 1911.05379.

30 J. R. Kennedy, P. Adler, R. Dronskowski, and A. Simon, Inorg. Chem. **35**, 2276 (1996).

31 C. M. Pasco, I. El Baggari, E. Bianco, L. F. Kourkoutis, and T. M. McQueen, ACS Nano **13**, 9457 (2019).

32 S. N. Magonov, P. Zoennchen, H. Rotter, H. J. Cantow, G. Thiele, J. Ren, and M. H. Whangbo, J. Am. Chem. Soc. **115**, 2495 (1993).

33 H. K. Mao, X. J. Chen, Y. Ding, B. Li, and L. Wang, Rev. Mod. Phys. **90**, 015007 (2018).

34 Y. Ma, M. Eremets, A. R. Oganov, Y. Xie, I. Trojan, S. Medvedev, A. O. Lyakhov, M. Valle, and V. Prakapenka, Nature **458**, 182 (2009), arXiv: 0911.3190.

35 C. Prescher, and V. B. Prakapenka, High Pressure Res. **35**, 223 (2015).

36 J. Rodríguez-Carvajal, Phys. B-Condensed Matter **192**, 55 (1993).

37 T. Ohsaka, F. Izumi, and Y. Fujiki, J. Raman Spectrosc. **7**, 321 (1978).

38 X. Fontané, V. Izquierdo-Roca, E. Saucedo, S. Schorr, V. O. Yukhymchuk, M. Y. Valakh, A. Pérez-Rodríguez, and J. R. Morante, J. Alloy Compd. **539**, 190 (2012).

39 N. Wada, S. A. Solin, J. Wong, and S. Prochazka, J. Non-Crystalline Solids **43**, 7 (1981).

40 Y. Liu, H. Wang, G. Chen, Y. D. Zhou, B. Y. Gu, and B. Q. Hu, J. Appl. Phys. **64**, 4651 (1988).

41 B. Das, M. V. Reddy, C. Krishnamoorthi, S. Tripathy, R. Mahendiran, G. V. S. Rao, and B. V. R. Chowdari, Electrochim. Acta **54**, 3360 (2009).

42 P. Müller, R. Hackl, R. Kaiser, N. Nücker, and A. Müller, Phys. B **135**, 355 (1985).

43 J. F. Cornwell, *Group Theory in Physics* (Academic, Press & World Scientific, Singapore, 1985).

44 Z. Zhao, H. Zhang, H. Yuan, S. Wang, Y. Lin, Q. Zeng, G. Xu, Z. Liu, G. K. Solanki, K. D. Patel, Y. Cui, H. Y. Hwang, and W. L. Mao, Nat. Commun. **6**, 7312 (2015), arXiv: 1504.08077.

45 A. Jaffe, Y. Lin, W. L. Mao, and H. I. Karunadasa, J. Am. Chem. Soc. **139**, 4330 (2017).

46 Z. Zhao, S. Wang, A. R. Oganov, P. Chen, Z. Liu, and W. L. Mao, Phys. Rev. B **89**, 180102 (2014).

47 L. Zhang, C. Liu, L. Wang, C. Liu, K. Wang, and B. Zou, Angew. Chem. Int. Ed. **57**, 11213 (2018).

48 Y. Fang, L. Zhang, Y. Yu, X. Yang, K. Wang, and B. Zou, CCS Chem. **2**, 2203 (2020).

49 Y. Ai, Y. Li, M. H. Y. Chan, G. Xiao, B. Zou, and V. W. W. Yam, J. Am. Chem. Soc. **143**, 10659 (2021).

50 Y. Liu, Q. Zeng, B. Zou, Y. Liu, B. Xu, and W. Tian, Angew. Chem. Int. Ed. **57**, 15670 (2018).